Supplementary Information

PVDF nanofiber separator with $LiNO_3$ enabling sustained additive release for dendrite-suppressed anode-free lithium metal batteries

Aldan Hadziq Haidar [a], Naufal Hanif Hawari [b, c], Dian Anggreini [a], Febri Baskoro [a], Ning Ding [c], Qingyu Yan [b], and Afriyanti Sumboja [a,*]

[a] Material Science and Engineering Research Group, Faculty of Mechanical and Aerospace Engineering, Institut Teknologi Bandung, Jl. Ganesa 10, Bandung 40132, Indonesia

[b] School of Materials Science and Engineering, Nanyang Technological University, Singapore 639798, Singapore

[c] Institute of Materials Research and Engineering (IMRE), Agency for Science, Technology and Research (A*STAR), 2 Fusionopolis Way, Innovis #08-03, Singapore 138634, Republic of Singapore

[*] Corresponding author: sumboja@itb.ac.id

Experimental Section

Preparation of PP/PVDF/$LiNO_3$ separator: PP/PVDF and PP/PVDF/$LiNO_3$ separator was prepared by electrospinning. The electrospinning solution was prepared by dissolving PVDF (polyvinylidene fluoride, HSV900/SOLVAY 5130, 0.47 g) in N,N-dimethylformamide (DMF, Sigma-Aldrich, 5 mL), followed by addition of $LiNO_3$ (lithium nitrate, Sigma-Aldrich, 0.47 g). This corresponds to PVDF and $LiNO_3$ each at 10 wt.% relative to the DMF mass used**.** The mixture was processed using a planetary mixer (SK-300SII, Kakuhunter) at 2000 rpm for 1 h until visually uniform (no visible precipitation) prior to electrospinning. Syringe with an 18-gauge needle was connected to electrospinning machine (Spinbox, Bionicia) with a rotating drum collector. Polypropylene separator (PP, Celgard 2500) used as the substrate is wrapped on the collector. For the electrospinning, high voltage of 15 kV was applied between the needle and the PP separator on rotation drum (rotation speed: 1000 rpm; distance: 15 cm), and injection speed of 0.02 ml min^{-1} (total volume of solution dispensed: 0.3 ml). In order to exclude the interference of H_2O on the stability of lithium nitrate, the air humidity was reduced to below 40 % using a dehumidifier before spinning. The PP/PVDF/$LiNO_3$ separator was dried at 60 °C for 12 h under vacuum conditions to remove residual solvent. It was then sectioned into 16 mm diameter circles and ready for cell assembly.

Materials and Postmortem Characterization: Scanning Electron Microscope (SEM, Hitachi SU3500) was used to examine surface and cross-section morphology of separators. Transmission Electron Microscope (TEM, JEOL 2100F) were used to examine the crystal cluster of PVDF/$LiNO_3$ nanofiber and its elemental composition. Fourier Transform-Infrared Spectroscopy (FTIR) measurements were completed on FTIR Bruker Alpha II. XRD patterns were measured on Bruker D8 advance diffractometer with Cu Kα radiation. UV–Vis spectroscopy was performed using a Thermo Fisher Scientific GENESYS 150. For post-cycling measurements, electrolyte (50 µL) was collected from disassembled coin cells after 1, 3, and 10 cycles and diluted with 300 µL carbonate electrolyte solvent. The diluted solutions (350 µL) were transferred into 350 µL microcuvettes and measured by UV–Vis spectroscopy. Tensile strength of the separator membranes was evaluated on a universal testing machine (UCT-5T, Oriented) equipped with a 100 kgf load cell, operated at a crosshead speed of 10 mm min^{-1}, with samples tested along the machine direction. XPS characterization was conducted on Kratos AXIS Ultra DLD using Al (Kα) source and argon ion sputter gun. Binding energy values of all XPS data were referenced to C 1s peak (284.8 eV). All the electrodes after cycling were rinsed with dimethyl carbonate (DMC, Sigma-Aldrich) several times to remove any residual salts and dried under vacuum before characterizations. For postmortem characterization, coin cells were disassembled inside glovebox (Kiyon KK-011AS) in argon atmosphere with O_2 and H_2O concentrations

below 0.5 ppm. All electrodes after cycling were washed using dimethyl carbonate (DMC, Sigma-Aldrich) for 15 minutes with 4 repetitions. Washed electrodes were then dried overnight in vacuum condition. Lithium plating morphology on the electrodes was observed using Scanning Electron Microscopy (SEM, JEOL JCM7000). Electrodes were exposed to ambient air for less than 1 minute during the transfer to the SEM vacuum chamber.

Coin Cell fabrication: Electrochemical tests were investigated by assembling the separators in a coin-cell (CR2032) in Argon filled glovebox (Kiyon KK-011AS) with O_2 and H_2O concentrations below 0.5 ppm. 1 M lithium hexafluorophosphate ($LiPF_6$) in ethylene carbonate (EC) / diethyl carbonate (DEC) (1 : 1 vol) with 10% fluoroethylene carbonate (FEC) was used as electrolyte for all data. The electrolyte volume per cell was maintained 130 µL unless otherwise specified. Copper foil and separator were cut into circles with diameters of 14 mm and 16 mm respectively. Lithium metal (thickness 750 µm) was used for Li||Cu asymmetric cell, Li symmetric cells, and Li||NMC asymmetric cells. NMC622 cathode was fabricated using a mixture of NMC622 powder (Shandong Gelon LIB Co.), PVDF (HSV900/SOLVAY 5130), and C65 at mass ratio of 90:5:5 using n-methyl-2-pyrollidone (NMP, sigma aldrich) as solvent. Slurry was coated on aluminum current collector using doctor blade with thickness of 300 µm. Then, cathode dried at 80 °C for 12 hours in vacuum. After that, the cathode was punched into circles with diameter of 12 mm, with active material mass loading of ≈ 10 mg cm^{-2} and adjusted for full-cells with different N/P ratio.

Electrochemical measurements: All the charge discharge test for Li||Li symmetric cells, Li||Cu asymmetric cells, Li||NMC cells, and Cu||NMC cells were performed using Neware BTS4000 battery tester. The Li||Cu cells were tested at a current rate of 1 mA cm^{-2} with upper cutoff voltage of 1 V and maximum capacity of 1 mAh cm^{-2}. The Li||NMC cells and Cu||NMC cells were performed at different current densities at 25 °C within the voltage range of 3–4.3 V. Electrochemical impedance spectroscopy (EIS) measurements were carried over 100 kHz to 10 mHz with amplitude 10 mV (Autolab PGSTAT302N, Metrohm). Tafel curve was tested with a galvanostat/potentiostat (Corrtest) in the voltage range –0.1 to 0.1 V at scan rates of 0.1 mV s^{-1} with Li||Cu configuration cell. Ionic conductivity was tested by AC Impedance with configuration of the stainless-steel SS|separator|SS. The ionic conductivity (σ) of the electrolytes using different separators were calculated using Equation S1:

$$\sigma = \frac{L}{R_b S} \quad \textbf{Equation S1}$$

Where L is the thickness of the separators, R_b is the bulk impedance determined from the EIS plot, and S is the effective contact area between the separators and the stainless-steel electrode, respectively. The Li^+ migration number (t_{Li^+}) calculation was conducted in Li||Li symmetric cells with potential applied for 8000 s and calculated using Equation S2:

$$t_{Li^+} = \frac{I_s(\Delta V - I_0 R_0)}{I_0(\Delta V - I_s R_s)} \quad \textbf{Equation S2}$$

Where ΔV (10 mV) is the potential applied. I_0 and I_s are the initial state current and steady-state current, respectively. R_0 and R_s are the initial state resistance and steady-state resistance, respectively. The Li Coulombic Efficiency (CE) of the Li||Cu cells assembled with different separators were evaluated by Aurbach method, where Li reservoir with an areal capacity of 5.0 mAh cm^{-2} was first deposited on Cu foil at 1 mA cm^{-2}, followed by 10 cycles of plating/striping at a current density of 1 mA cm^{-2} with a capacity of 1 mAh cm^{-2}, and finally stripping to 1 V. The average CE was calculated by Equation S3:

$$Average\ CE\ = \frac{Q_S + Q_C n}{Q_P + Q_C n} \quad \textbf{Equation S3}$$

where Q_S is the final stripping capacity, Q_P is the initial plating capacity (5 mAh cm^{-2}), Q_C is the constant plating/stripping capacity for each cycle (1 mAh cm^{-2}), and n is the number of cycle (10).

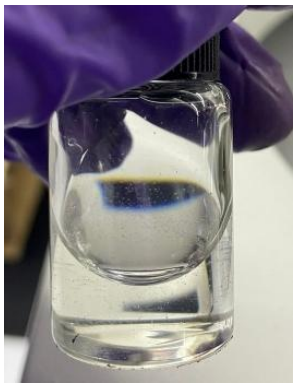

Fig. S1 Visually uniform PVDF/$LiNO_3$/DMF electrospinning solution (10 wt.% PVDF and 10 wt.% $LiNO_3$ relative to DMF) before electrospinning.

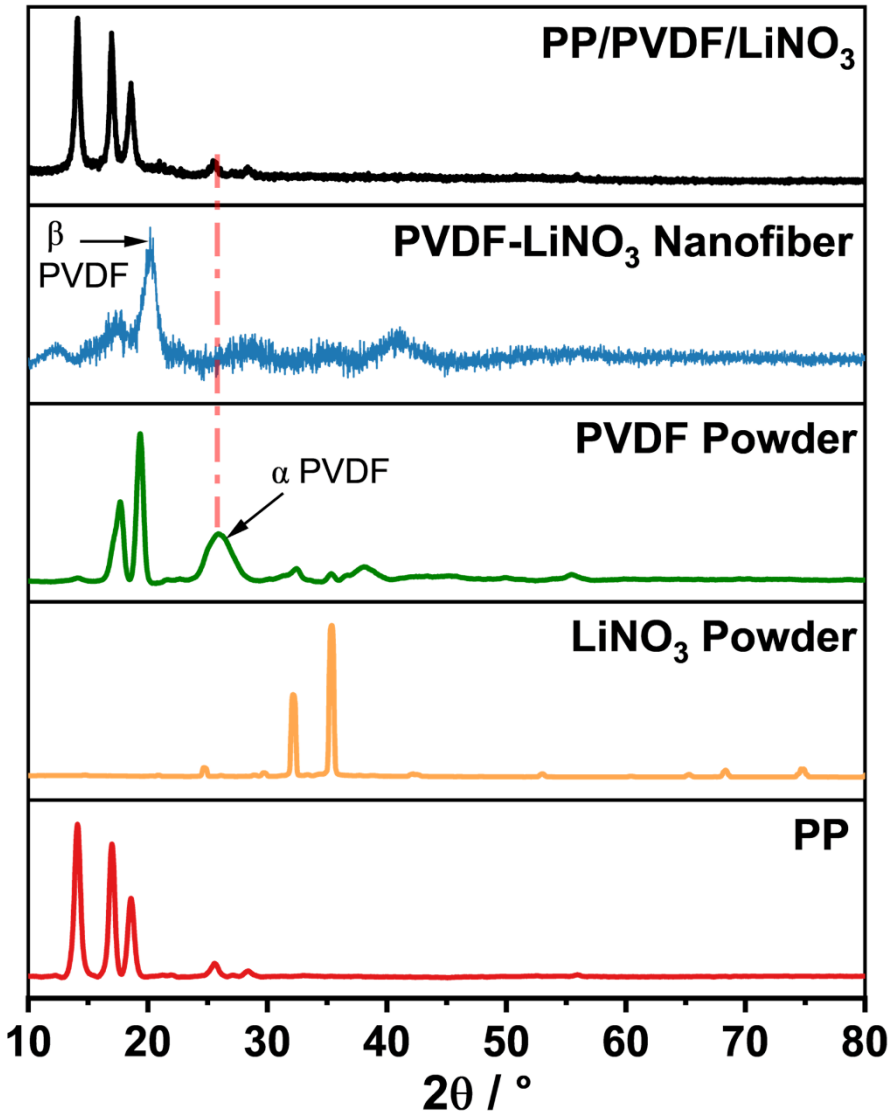

Fig. S2 The XRD pattern of PP/PVDF/$LiNO_3$ separator, PVDF-$LiNO_3$ nanofiber, PVDF Powder, $LiNO_3$

Equation S4. Calculation of β phase PVDF using FTIR data

$$F(\beta) = \frac{A_\beta}{(\frac{K_\beta}{K_\alpha})\, A_\alpha + A_\beta} \times 100\%$$

$F(\beta) = \beta\ phase\ content$
$A_\beta = \beta\ phase\ absorbance\ at\ 840\ cm^{-1}$
$A_\alpha = \alpha\ phase\ absorbance\ at\ 766\ cm^{-1}$
$K_\alpha = Absorptioncoefficient (6.1 \times 10^4 cm^2\ mol^{-1})$
$K_\beta = Absorption\ coefficient\ (7.7 \times 10^4 cm^2\ mol^{-1})$

Table S1 Comparison of β phase content

Sample	$A_{\alpha\,766}$	$A_{\beta\,840}$	$A_{\gamma\,1234}$	$A_{\beta\,1275}$	$F(\beta)$
PVDF	0.0087	0.0974	0.0574	0.0586	89.8%
PP/PVDF/$LiNO_3$	0.0008	0.0347	0.0427	0.0739	97.1%

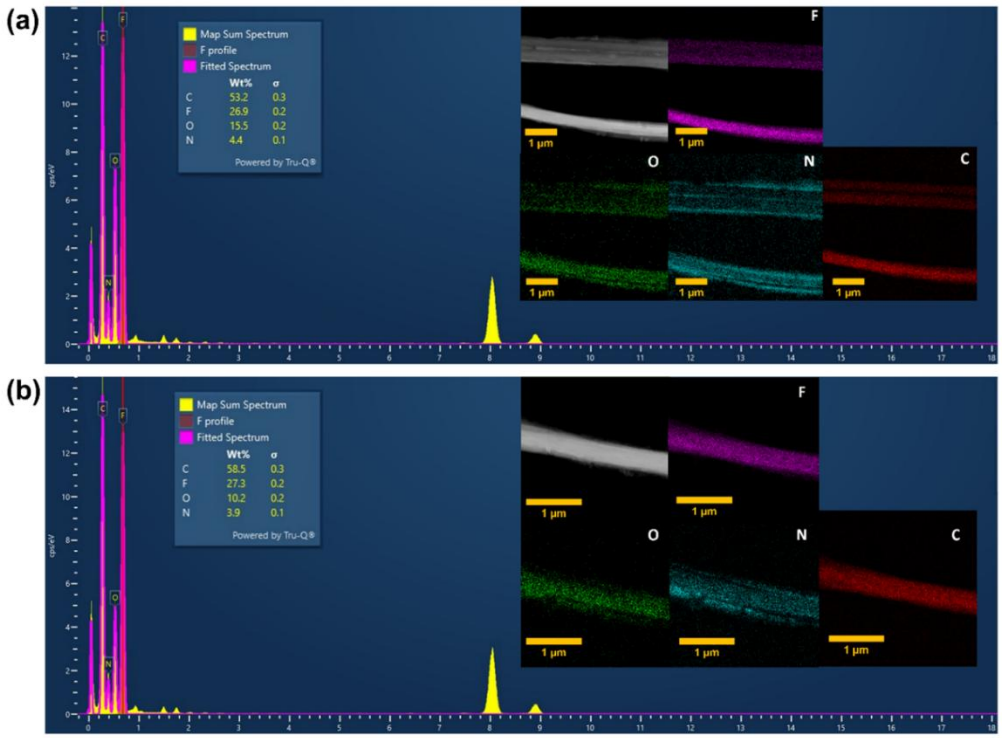

Fig. S3 Multi-location STEM–EDS analysis of electrospun PVDF/$LiNO_3$ fibers. (a–b) STEM–EDS spectra (semi-quantitative wt.%) and corresponding elemental maps collected from two spatially separated fiber regions. The C and F maps outline the PVDF fiber morphology, while N and O maps show nitrate-related elemental signals co-localized with the fibers across multiple locations.

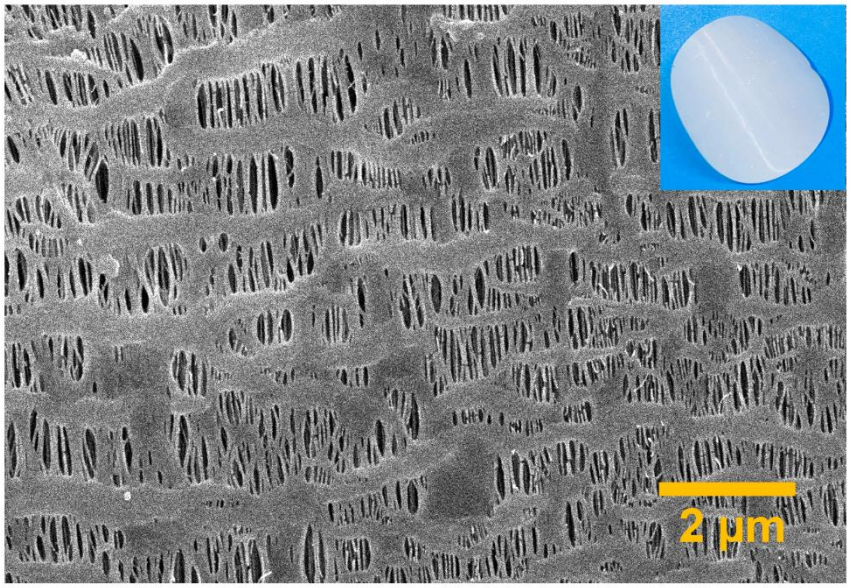

Fig. S4 Top-view SEM image of the PP separator (inset: corresponding photograph)

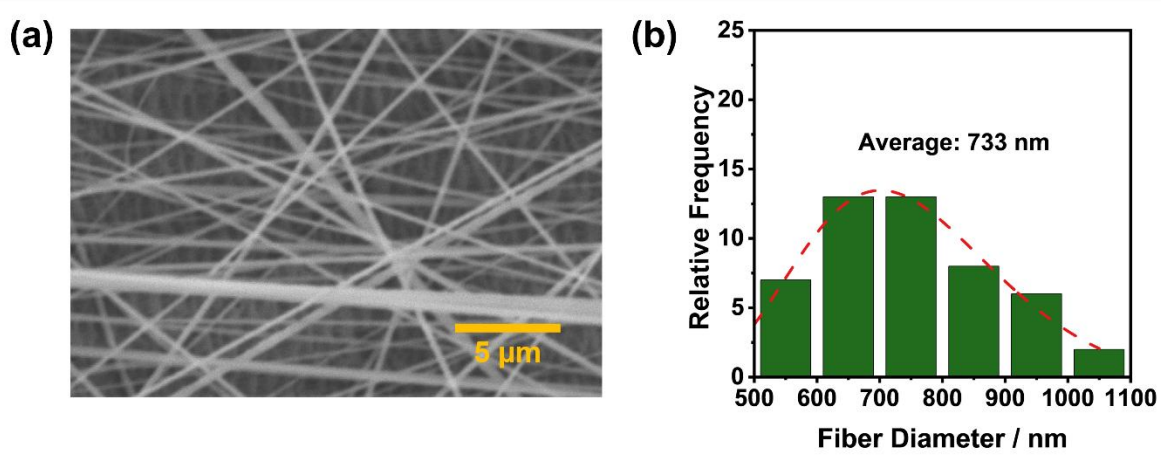

Fig. S5 (a) Top-view SEM image of the electrospun PVDF nanofiber layer on PP and (b) fiber diameter distribution of the electrospun PVDF nanofibers.

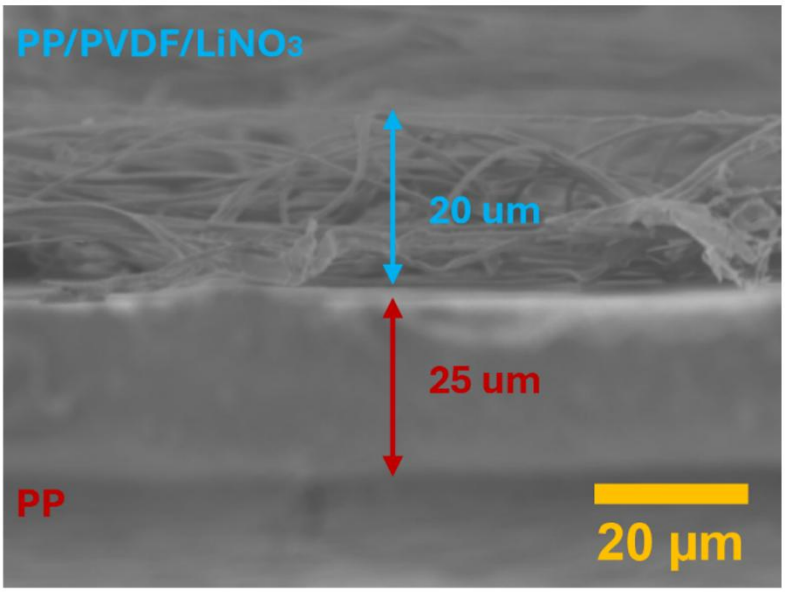

Fig. S6 Cross-section SEM views of PP/PVDF/$LiNO_3$ separator

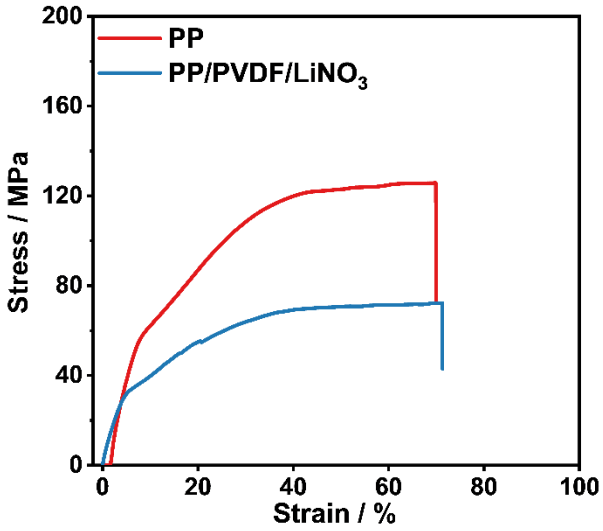

Fig. S7 Tensile stress–strain curves of PP and PP/PVDF/$LiNO_3$ separators.

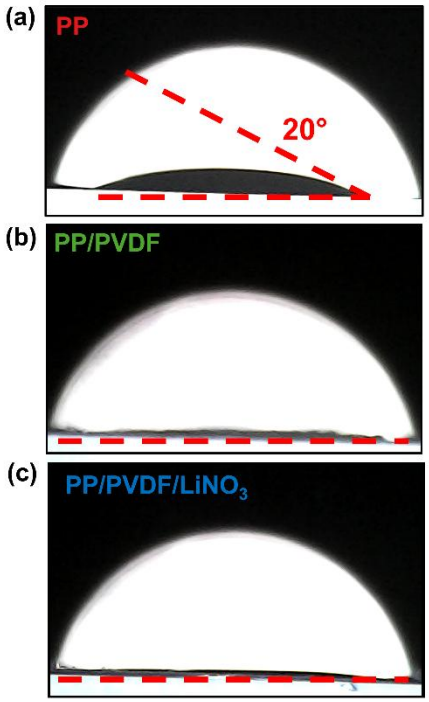

Fig. S8 Contact angle measurements of (a) PP separator, (b) PP/PVDF separator, and (c) PP/PVDF/$LiNO_3$ separator

Table S2 Physical properties of PP, PP/PVDF, and PP/PVDF/$LiNO_3$ separator

Sample	Weight (mg)	Thickness (μm)	Electrolyte Uptake (%)
PP	2.1	25	124 ± 19.44
PP/PVDF	2.4	40	296 ± 11.41
PP/PVDF/$LiNO_3$	2.6	45	317 ± 17.52

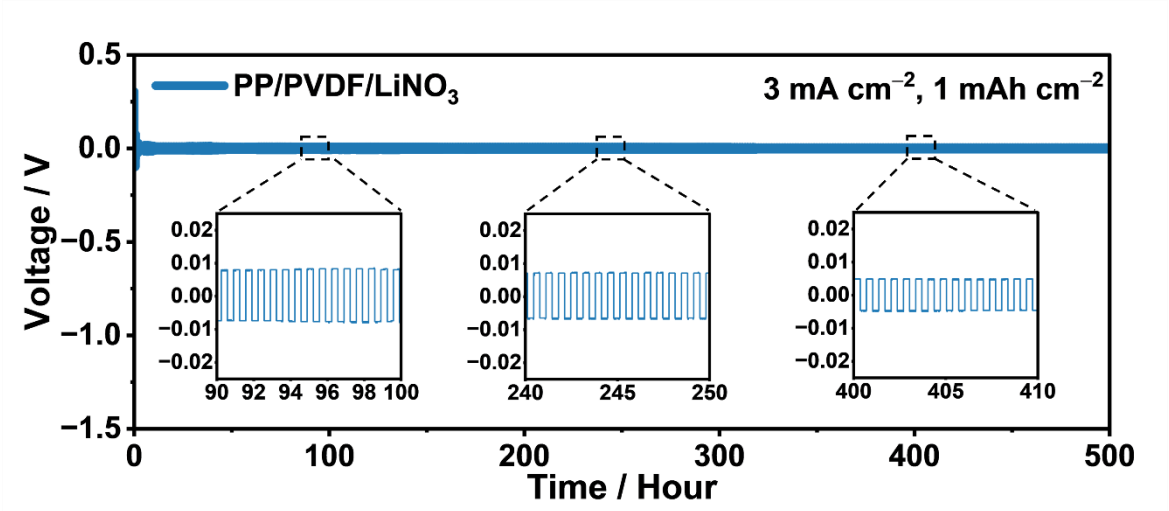

Fig. S9 Zoomed-in voltage profiles of the PP/PVDF/$LiNO_3$ symmetric cell during galvanostatic cycling at 3 mA cm^{-2} and 1 mAh cm^{-2}, highlighting a low overpotential of ~14 mV.

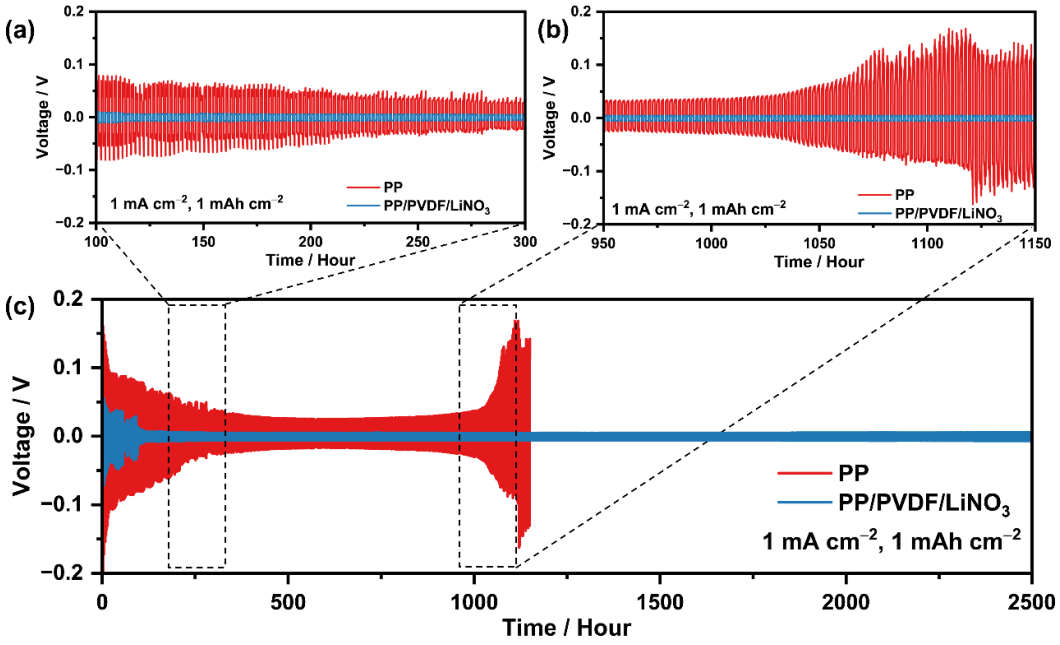

Fig. S10 Long-term Li plating/stripping stability of Li||Li symmetric cells with PP and PP/PVDF/$LiNO_3$ separators at a current density of 1 mA cm^{-2} and an areal capacity of 1 mAh cm^{-2}. (a,b) Enlarged voltage profiles corresponding to the highlighted time windows. (c) Full voltage–time profiles over long-term cycling.

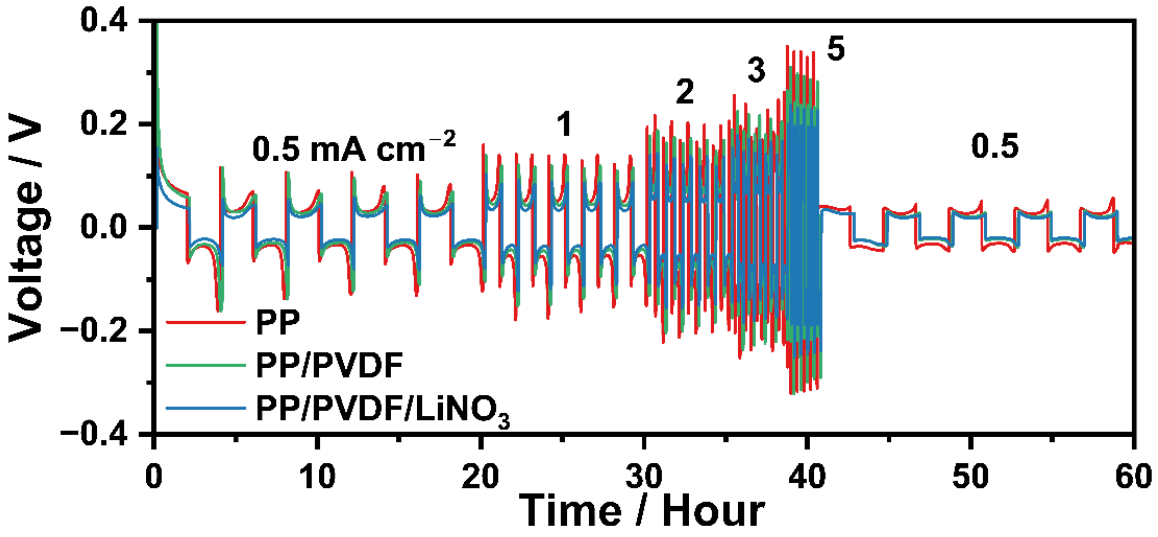

Fig. S11 Rate performance of Li||Li symmetric cells using PP, PP/PVDF, and PP/PVDF/$LiNO_3$ separators under stepwise current-density cycling.

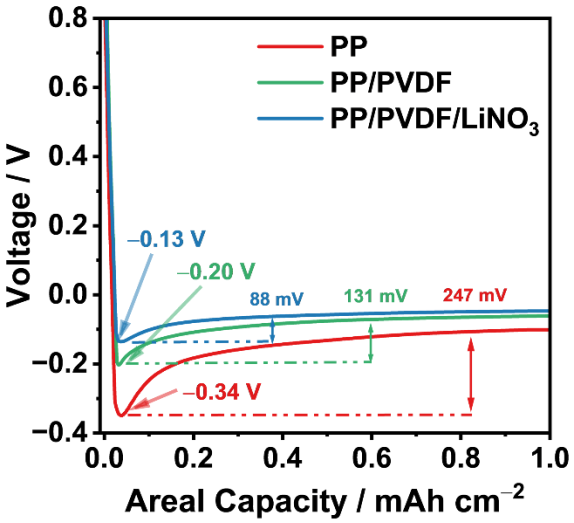

Fig. S12 Initial Li plating profiles highlighting nucleation overpotential in Li||Cu cells with PP, PP/PVDF, and PP/PVDF/$LiNO_3$ separators (1 mA cm^{-2}).

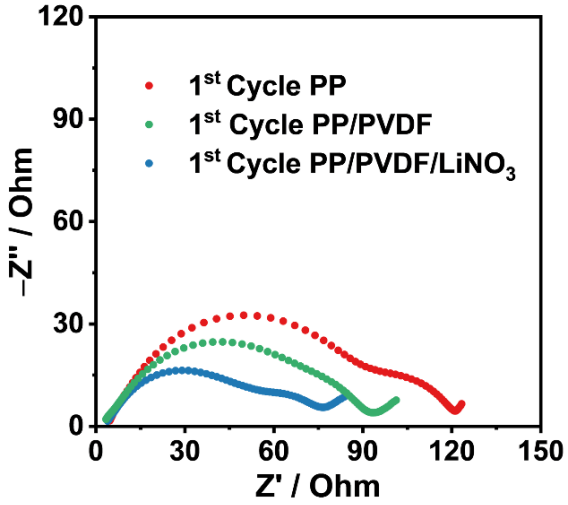

Fig. S13 Half-cell first cycle electrochemical impedance spectra data of PP, PP/PVDF, and PP/PVDF/$LiNO_3$ separator.

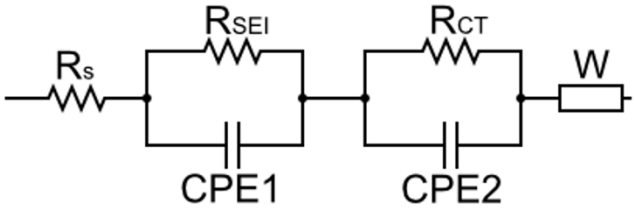

Fig. S14 Equivalent circuit model for EIS analysis

Table S3 Fitting results of the electrochemical impedance spectra

Sample	R_S	R_{SEI}	R_{CT}	Error X^2
PP	4	96	18	0.02
PP/PVDF	3	72	16	0.02
PP/PVDF/$LiNO_3$	3	55	15	0.02

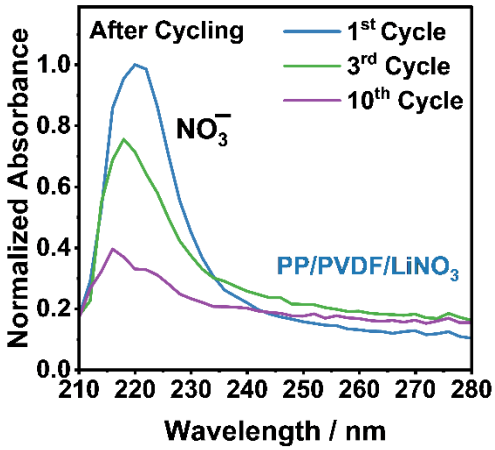

Fig. S15 Post-cycling UV–Vis spectra (after cycles 1, 3, and 10) showing a progressive decrease in the NO_3^- absorption band.

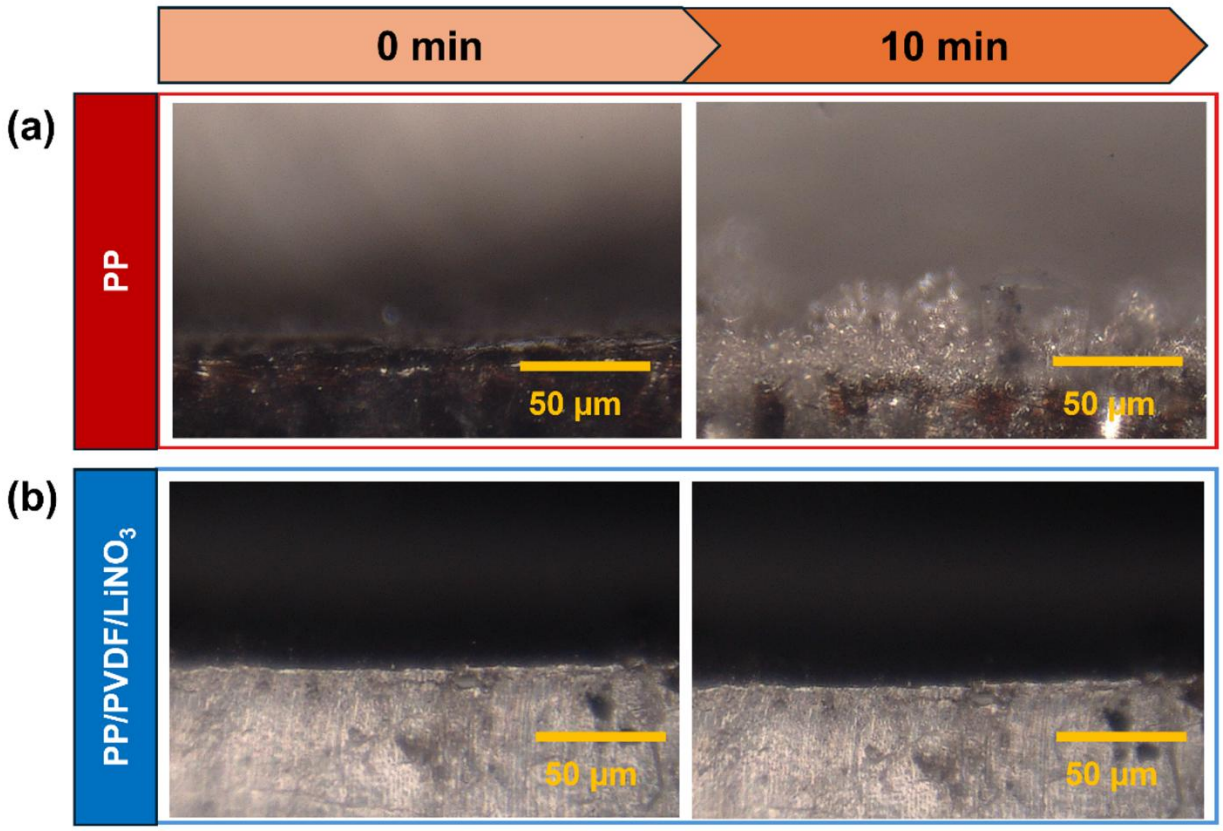

Fig. S16 In-situ optical microscopy observation of lithium deposition and dendrite growth from (a) PP separator and (b) PP/PVDF/$LiNO_3$ after 10 minutes at current density 10 mA cm^{-2}

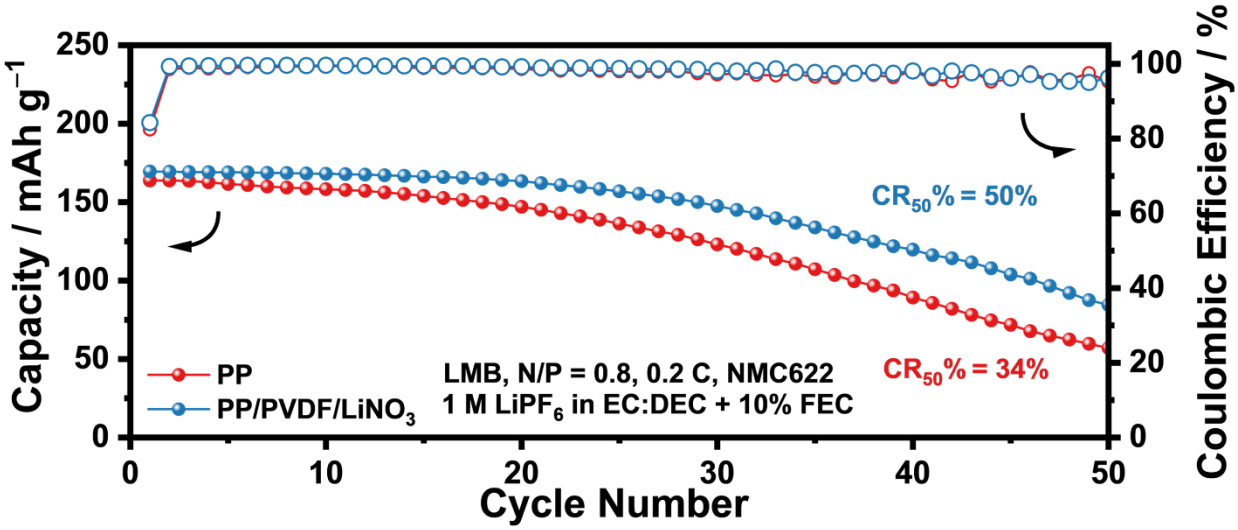

Fig. S17 Full-cell (LMB) performance results of cells utilizing llithium metal with N/P ratio of 0.8 at 0.2C

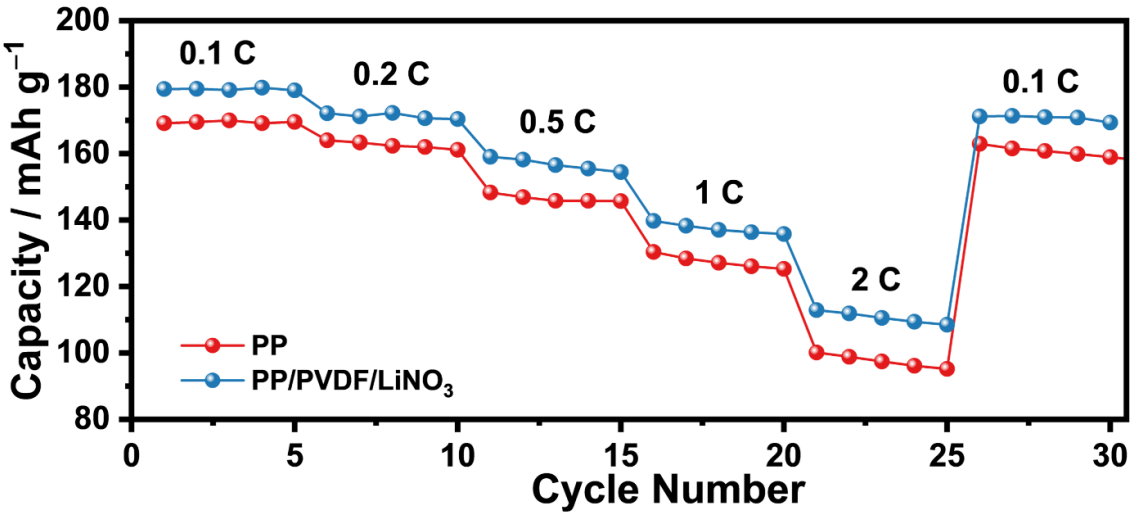

Fig. S18 Rate performance of Li||NCM622 (LMB) cells using different separators.

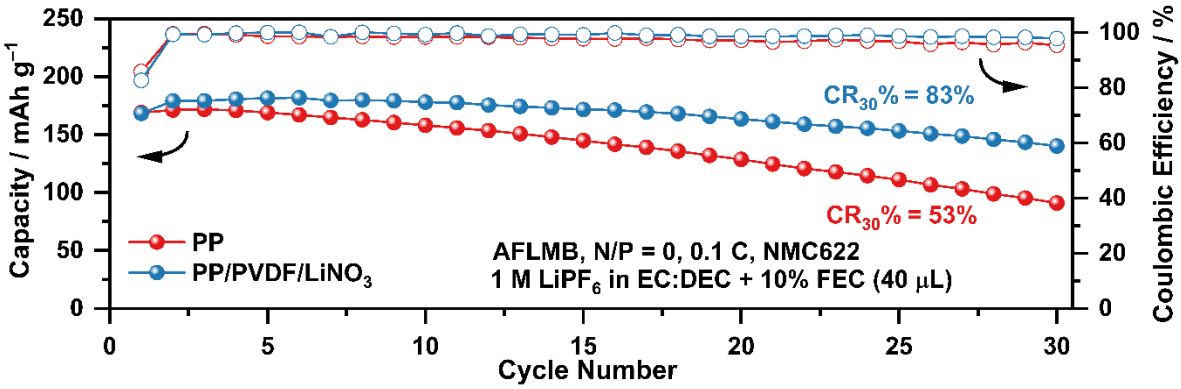

Fig. S19 Cycling performance of Cu||NMC622 AFLMBs under restricted electrolyte conditions. Capacity retention and Coulombic efficiency of cells using PP/PVDF/$LiNO_3$ and PP separators with an electrolyte volume of 40 μL, demonstrating sustained performance advantages under lean-electrolyte operation.

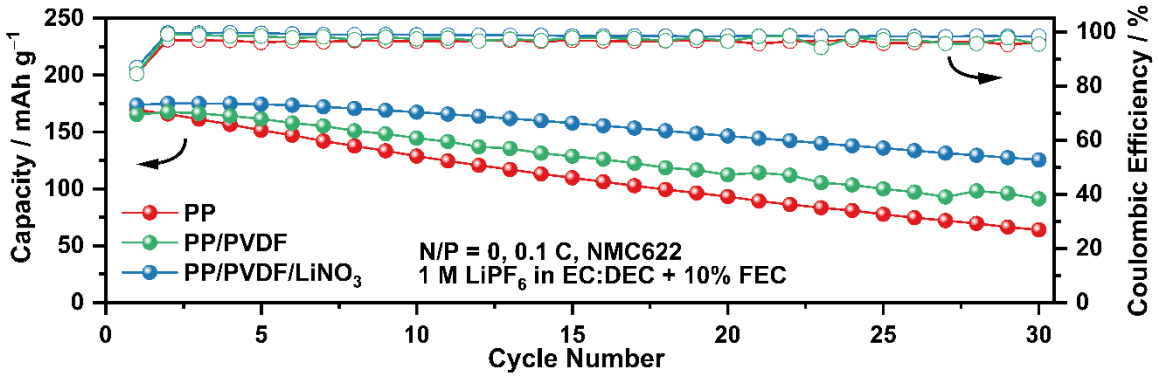

Fig. S20 Cycling performance of anode-free full cells (AFLMBs) with zero-excess lithium at 0.1 C using PP, PP/PVDF, and PP/PVDF/$LiNO_3$ separators, showing capacity retention and Coulombic efficiency.

Table S4 Comparison of cycling stability in full cells (LMB) with different modifications at various N/P ratio

Modification Method	Electrolyte	N/P ratio	Areal capacity (mAh cm^{-2})	Cycling stability	Ref.
PP/PVDF/$LiNO_3$ Separator (Electrospinning)	1 M $LiPF_6$ in EC/DEC (1:1 v/v) + 10% FEC	1.8	2 (NMC622)	83% after 100 cycles at 0.1 C	This work
CAM Separator (Coating)	1 M $LiPF_6$ in EC/DEC (1:2 v/v) + 10% FEC	5	0.7 (NMC622)	80% after 100 cycles at 0.5 C	1
Tungsten (W/PE) Separator (Sputtering)	1 M $LiPF_6$ in EC/DEC (1:1 v/v) + 10% FEC	1	3 (NMC811)	82% after 118 cycles at 0.3 C	2
High Polarity Beta PVDF Cu (Coating)	1 M LiTFSI (1:1 v/v) + 3% $LiNO_3$	0.86	1.47 (LFP)	65% after 100 cycles at 0.3 C	3
3D Skeleton FNCS@CF (Dip coating)	1 M $LiPF_6$ in EC/DEC (1:1 v/v)	1.5	3.42 (NMC532)	77% after 100 cycles at 0.2 C	4
3D Li-CFs@GZnO (Electrospinning)	1 M $LiPF_6$ in EC/DEC/DMC (1:1:1 v/v/v) + 5% FEC	2	2 (NMC811)	91% after 100 cycles at 0.2 C	5
Phoshphorene Nanoribbon (Coating)	1 M $LiPF_6$ in EC/DEC (1:1 v/v)	3.5	2 (LFP)	74% after 100 cycles at 0.1 C	6
PAN $AgNO_3$ nanofiber Cu (Electrospinning)	1 M $LiPF_6$ in EC/DEC (1:1 v/v) + 5% FEC	4	1 (NC90)	84% after 100 cycles at 0.5 C	7
3D $AgNO_3$ PVDF Cu (Electrospinning)	1 M $LiPF_6$ in EC/DMC (1:1 v/v) + 5% FEC	3	1 (LFP)	86.3% after 100 cycles at 1 C	8
3D Li_2CO_3 PVDF Cu (Electrospinning)	4 M LiFSI in DME	2	2.6 (NMC622)	80.7% after 100 cycles at 0.2 C	9

Table S5 Comparative analysis of technical positioning, cost, safety, and processing requirements between PP/PVDF/$LiNO_3$ separator vs. advanced electrolyte strategies.

Category	Advanced Electrolyte (LHCE / Fluorinated Ethers)	This Work (PP/PVDF/$LiNO_3$ Separator / Carbonate)
Technical Positioning	Bulk electrolyte modification; solvation sheath engineering	Interfacial engineering via separator-integrated functional layer
Cost (Active Materials)	High, dominated by fluorinated diluents and high salt content	Low, achieved using minimal $LiNO_3$ inventory and commercial PVDF
Safety Considerations	Ether-based components with high volatility and flammability; oxidative stability concerns at high voltage	Carbonate-based electrolyte retained; non-volatile PVDF matrix with confined additive delivery
Mechanical Contribution	No intrinsic mechanical or interfacial regulation (liquid phase-dominated behaviour	Active regulation via β-phase PVDF and SEI stabilization
Processing and Scalability	Requires electrolyte re-optimization due to high viscosity and altered wetting behavior	Compatible with established separator coating and roll-to-roll processing

Table S6 Comparison of cycling stability in full cells anode-free (AFLMB) with different modifications

Modification Method	Electrolyte	Areal Capacity (mAh cm^{-2})	Cycling stability	Ref.
PP/PVDF/$LiNO_3$ (Separator)	1 M $LiPF_6$ in EC/DEC (1:1 v/v) + 10% FEC	2 (NMC622)	54% after 50 cycles at 0.1 C	This work
Graphene Oxide Coated Cu (Current Collector)	1 M $LiPF_6$ in EC/DEC (1:1 v/v) + 5% FEC	1.8 (NMC111)	44% after 50 cycles at 0.2 C	10
PVDF-HFP/LASGP (Gel Polymer Electrolyte)	1 M $LiPF_6$ in EC/DEC	2 (NMC333)	42% after 65 cycles at 0.1 C	11
$LiPF_6$ / FEC (Electrolyte Additive)	1 M $LiPF_6$ in EC//DMC/FEC (1:1:2 v/v/v)	2 (NMC111)	40% after 50 cycles at 0.1 C	12
Cu@β-PVDF fiber (Current Collector)	1 M $LiPF_6$ in EC/DEC	1.3 (NMC111)	61% after 30 cycles at 0.1 C	13
Al_2O_3/PAN (Current Collector)	1 M $LiPF_6$ in EC/DEC (1:1 v/v) + 25% KNO_3	2.3 (NMC333)	30% after 82 cycles at 0.2 C	14
DDEDF (Electrolyte)	1 M LiDFOB in EC/DMC (1:1, v/v %) + 1 wt% LiDFP +1 wt% FEC	1.5 (NMC811)	40% after 100 cycles at 0.2 C	15
LiDFOB + $LiPF_6$ DEC (Electrolyte)	1 M LiDFOB + 0.05 M $LiPF_6$ in FEC TTE DEC (2:2:1 v/v/v)	2 (NMC532)	45% after 35 cycles at 0.2 C	16
3D Li_2CO_3/PVDF Cu (Current Collector)	4 M LiFSI in DME	2.6 (NMC622)	70% after 30 cycles at 0.2 C	9
$LiNO_3$-Modified PP (Separator)	1 M $LiPF_6$ in EC/EMC (3:7 wt/wt)	2.3 (NMC622)	62% after 50 cycles at 0.2 C 40°C	17
LLCZN/PVDF/$LiClO_4$ (Current Collector)	1 M $LiPF_6$ in EC/DEC (1:1 v/v)	2.1 (NMC111)	58% after 50 cycles 0.2 C	18

Table S7 Comparison of cycling stability in full cells (LMB) with sustained additive release mechanism

Modification Method	Additive	Electrolyte	Areal Capacity (mAh cm^{-2})	Cycling stability	Ref.
PP/PVDF/$LiNO_3$ Separator (Electrospun)	$LiNO_3$	1 M $LiPF_6$ in EC/DEC (1:1 v/v) + 10% FEC	2 (NMC622)	83% after 100 cycles at 0.1 C	This work
$AgNO_3$/PAN (Electrospun)	$AgNO_3$	1 M $LiPF_6$ in EC/DEC/FEC (45:45:10 v/v/v)	1.8 (LCO)	85% after 100 cycles at 0.5 C	19
Biscuit PP/ $LiNO_3$/ Separator (Coating)	$LiNO_3$	1 M $LiPF_6$ in EC/DEC (1:1 v/v)	2.1 (NMC811)	70% after 60 cycles at 0.5 C	20
$LiNO_3$/PAN (Electrospun)	$LiNO_3$	1 M $LiPF_6$ in EC/DEC/EMC (1:1:1 v/v/v)	4.6 (NMC622)	71% after 160 cycles at 0.2 C	21

Supplementary reference

1. Y. Yang, S. Yao, Y. Wu, J. Ding, Z. Liang, F. Li, M. Zhu and J. Liu, *Nano Letters*, 2023, **23**, 5061-5069.
2. J. Oh, J. L. Frank, R. A. Leising, H. Kim, J. Kim, M. Kim and J. W. Choi, *Energy Environ. Sci.*, 2025, **18**, 7504-7513.
3. J. Luo, C.-C. Fang and N.-L. Wu, *Adv. Energy Mater.*, 2018, **8**, 1701482.
4. H. Gan, R. Wang, J. Wu, H. Chen, R. Li and H. Liu, *ACS Appl. Mater. Interfaces.*, 2021, **13**, 37162-37171.
5. Z. Xiao, D. Han, Y. Fu, K. Xie, W. Tian, C. Shu, K. Xi, C. Peng, Y. Wu, S. Dou and W. Tang, *Chem. Eng. J*, 2024, **480**, 148029.
6. W. Yu, J. Yang, J. Li, K. Zhang, H. Xu, X. Zhou, W. Chen and K. P. Loh, *Adv. Mater.*, 2021, **33**, 2102083.
7. Q. Ran, L. Wang, L. Li, Y. Zhao, Z. Lu, S. Chen, J. Zou, P. Chen, J. Gao and X. Niu, *Chem. Eng. J*, 2021, **426**, 130780.
8. Y. Zhao, L. Wang, J. Zou, Q. Ran, L. Li, P. Chen, H. Yu, J. Gao and X. Niu, *J. Energy Chem.*, 2022, **65**, 666-673.
9. H. N. Hidayat, N. H. Hawari, A. H. Haidar, Q. Zhu, N. Ding, Q. Yan and A. Sumboja, *Nano Res.*, 2025, **18**, 94907781.
10. Z. T. Wondimkun, T. T. Beyene, M. A. Weret, N. A. Sahalie, C.-J. Huang, B. Thirumalraj, B. A. Jote, D. Wang, W.-N. Su, C.-H. Wang, G. Brunklaus, M. Winter and B.-J. Hwang, *J. Power Sources*, 2020, **450**, 227589.
11. H. G. Redda, Y. Nikodimos, W.-N. Su, R.-S. Chen, T. M. Hagos, H. K. Bezabh, H. H. Weldeyohannes and B. J. Hwang, *Mater. Today Energy*, 2022, **30**, 101141.
12. T. T. Hagos, B. Thirumalraj, C.-J. Huang, L. H. Abrha, T. M. Hagos, G. B. Berhe, H. K. Bezabh, J. Cherng, S.-F. Chiu, W.-N. Su and B.-J. Hwang, *ACS Appl. Mater. Interfaces.*, 2019, **11**, 9955-9963.
13. L. H. Abrha, Y. Nikodimos, H. H. Weldeyohannes, T. T. Hagos, D.-Y. Wang, C.-J. Huang, S.-K. Jiang, S.-H. Wu, W.-N. Su, M.-C. Tsai and B. J. Hwang, *ACS Appl. Energy Mater.*, 2021, **4**, 3240-3248.
14. N. A. Sahalie, Z. T. Wondimkun, W.-N. Su, M. A. Weret, F. W. Fenta, G. B. Berhe, C.-J. Huang, Y.-C. Hsu and B. J. Hwang, *ACS Appl. Energy Mater.*, 2020, **3**, 7666-7679.
15. K. Natarajan, S.-H. Wu, Y.-S. Wu, J.-K. Chang, R. Jose and C.-C. Yang, *J. Energy Storage.*, 2025, **109**, 115165.
16. B. A. Jote, T. T. Beyene, N. A. Sahalie, M. A. Weret, B. W. Olbassa, Z. T. Wondimkun, G. B. Berhe, C.-J. Huang, W.-N. Su and B. J. Hwang, *J. Power Sources*, 2020, **461**, 228102.
17. S. Stuckenberg, M. M. Bela, C.-T. Lechtenfeld, M. Mense, V. Küpers, T. T. K. Ingber, M. Winter and M. C. Stan, *Small*, 2024, **20**, 2305203.
18. L. H. Abrha, T. A. Zegeye, T. T. Hagos, H. Sutiono, T. M. Hagos, G. B. Berhe, C.-J. Huang, S.-K. Jiang, W.-N. Su, Y.-W. Yang and B.-J. Hwang, *Electrochim. Acta.*, 2019, **325**, 134825.
19. H. Kang, T.-H. Kim, G. Hwang, G. H. Shin, J. Lee, G. Kim and E. Cho, *Chem. Eng. J*, 2024, **484**, 149510.
20. Y. Liu, X. Qin, D. Zhou, H. Xia, S. Zhang, G. Chen, F. Kang and B. Li, *Energy Storage Mater.*, 2020, **24**, 229-236.
21. K. Peng, X. Wang and X. Yan, *Chin.Chem. Lett.*, 2024, **35**, 109274.